

Adaptive and Compressive Beamforming Using Deep Learning for Medical Ultrasound

Shujaat Khan, Jaeyoung Huh, and Jong Chul Ye, *Fellow, IEEE*

Abstract—In ultrasound (US) imaging, various types of adaptive beamforming techniques have been investigated to improve the resolution and contrast-to-noise ratio of the delay and sum (DAS) beamformers. Unfortunately, the performance of these adaptive beamforming approaches degrade when the underlying model is not sufficiently accurate and the number of channels decreases. To address this problem, here we propose a deep learning-based beamformer to generate significantly improved images over widely varying measurement conditions and channel subsampling patterns. In particular, our deep neural network is designed to directly process full or sub-sampled radio-frequency (RF) data acquired at various subsampling rates and detector configurations so that it can generate high quality ultrasound images using a single beamformer. The origin of such input-dependent adaptivity is also theoretically analyzed. Experimental results using B-mode focused ultrasound confirm the efficacy of the proposed methods.

Index Terms—Ultrasound imaging, B-mode, beamforming, adaptive beamformer, Capon beamformer

I. INTRODUCTION

Excellent temporal resolution with reasonable image quality makes the ultrasound (US) modality a first choice for variety of clinical applications. Moreover, due to its non-invasive nature, US is an indispensable tool for some clinical applications such as cardiac, fetal imaging, etc.

In US, an image reconstruction is usually done by back-propagating the preprocessed measurement data and adding all the contributions. For example, in focused B-mode US imaging, the return echoes from individual scan lines are recorded by the receiver channels (Rx), after which a delay and sum (DAS) beamformer applies appropriate time-delays to the channel measurements and additively combines them for each depth to form an image at each scan line. Despite the simplicity, large number of receiver elements are often necessary in DAS beamformer to improve the image quality by reducing the side lobes. Moreover, to calculate accurate time delay, sufficiently large bandwidth transducers are required.

To deal with unfavorable acquisition conditions, various adaptive beamforming techniques have been developed over the several decades [1]–[9]. The main idea of adaptive beamforming is to change the receive aperture weights based on the received data statistics to improve the resolution and enhance the contrast. One of the most extensively studied adaptive beamforming techniques is Capon beamforming, also known as the minimum variance (MV) beamforming [2]–[4]. The aperture weight of Capon beamformer is derived by

minimizing the side lobe while maintaining the gain in the look-ahead direction. Unfortunately, Capon beamforming is computationally heavy for practical use due to the calculation of the spatial covariance matrix of channel data and its inverse [5]. Moreover, the performance of Capon beamformer is dependent upon the accuracy of the covariance matrix estimate. To address these problems, many improved versions of MV beamformers have been proposed [4]–[7]. Some of the notable examples include the beamspace adaptive beamformer [6], multi-beam Capon based on multibeam covariance matrices [8], etc. In addition, a parametric form of iterative update covariance matrix calculation has been proposed instead of calculating the empirical covariance matrix [9].

On the other hand, compressive beamforming method have been also extensively investigated to reduce the data rate [10]. Specifically, high-quality ultrasound imaging demands for significantly high sampling rates, which eventually increases the volume of data transmitted from the system’s front end. Moreover, in 3-D ultrasound imaging, 2-D transducer arrays are used and more scan lines are needed, which leads to vastly increased amount of sampled data with respect to 2-D imaging. To achieve the aforementioned data rate reduction, random RF sub-sampling has been employed in various ultrasound imaging researches, e.g. [11], etc. Many researches also suggested the buffered probe sampling which can reduce the number of scan lines at the cost of complexity in probe design. Then specially designed compressive beamforming techniques were used to exploit the redundancy in the image to compensate for the reduced measurement data [10], [12]. Unfortunately, most of the existing compressive beamformers require either hardware changes [13] or computationally expensive optimization methods [10].

Recently, inspired by the tremendous success of deep learning, many researchers have investigated deep learning approaches for various inverse problems [14]–[25]. In US literature, the works in [26], [27] were among the first to apply deep learning approaches to US image reconstruction. In particular, Allman *et al* [26] proposed a machine learning method to identify and remove reflection artifacts in photo-acoustic channel data. Luchies and Byram [27] proposed a frequency domain deep learning method for suppressing off-axis scattering in ultrasound channel data. In [28], a deep neural network is designed to estimate the attenuation characteristics of sound in human body. In [29], [30], ultrasound image denoising method is proposed for the B-mode and single angle plane wave imaging. Rather than using deep neural network as a post processing method, the authors in [31]–[34] employed deep neural networks for the reconstruction

The authors are with the Department of Bio and Brain Engineering, Korea Advanced Institute of Science and Technology (KAIST), Daejeon 34141, Republic of Korea (e-mail: {shujaat,woori93,jong.ye}@kaist.ac.kr).

of high-quality US images from limited number of received RF data. For example, the work in [32] uses deep neural network for coherent compound imaging from small number of plane wave illumination. In focused B-mode ultrasound imaging, [31] employs the deep neural network to interpolate the missing RF-channel data with multiline acquisition for accelerated scanning.

While these recent deep neural network approaches provide impressive reconstruction performance, the designed neural network cannot completely replace a DAS beamformer, since they are designed as pre- or post- processing steps for specific acquisition scenarios and many of the works employ the standard DAS beamformer. Therefore, one of the most important contributions of this paper is to replace the DAS, adaptive, or compressive beamformers with a deep learning-based data-driven adaptive deep beamformer (DeepBF) so that a single DeepBF can generate high quality images robustly for various detector channel configurations. Moreover, unlike the MV beamformer that can be used only for uniform array, our DeepBF is designed for various detectors and RF subsampling schemes, in spite of significantly reduced runtime computational complexity. In contrast to [31], where the deep learning approach was developed to interpolate missing RF data to be used as input to the standard beamformer, the proposed method is a CNN-based beamforming pipeline, without requiring additional beamformer. Consequently, this approach is much simpler and can be easily incorporated to replace the standard beamforming pipeline. Despite the simplicity, our experiments show that direct reconstruction using the proposed DeepBF produces better results compared to [31].

The consistent performance improvement over widely varying subsampling rates using a single CNN may appear mysterious. Inspired by the recent theoretical understanding of deep convolutional framelets [35], [36], another important contribution of this paper is a detailed theoretical analysis to identify the origin of the input adaptivity and the performance improvement of DeepBF. Our theoretical analysis suggests that the deep learning-based beamformer may be the right direction for medical ultrasound.

After the initial work of this paper became available on Arxiv [37], a related work on deep learning based adaptive beamformer appeared [38]. In contrast to the proposed method, [38] is interested in estimating the adaptive beamformer weights using a deep neural network. Moreover, the results are only available for simple phantom data, the application of compressive beamforming was not considered, and the theoretical analysis to unveil why the deep learning beamformer works was not provided. Therefore, our work is more general and provides a systematic understanding in designing deep learning based beamformer.

This paper is organized as follows. In Section II, a brief survey of the existing adaptive beamforming methods are provided, which is followed by the detailed explanation of the proposed deep beamformer in Section III. Section IV then describes the data set and experimental setup. Experimental results are provided in Section V, which is followed by Discussion and Conclusions in Section VI and Section VII,

respectively.

II. MATHEMATICAL PRELIMINARIES

A. Notation

In this paper, the uppercase boldface letter such as \mathbf{X} , \mathbf{Y}_n are used to refer matrices and tensors, whereas the lowercase boldface letters such as \mathbf{x} , $\mathbf{y}_{l,n}$ represent the vector. Non-bold letters such as x , $v_{l,n}$ denote the scalars.

Measured RF data is a three-dimensional cube $\mathbf{X} \in \mathbb{R}^{L \times N \times E}$ from the B-mode ultrasound as shown in Fig. 1 (a), where L , N , and E denote the number of scan lines (or transmit events (TE)), depth planes, and the number of probe elements, respectively. The RF data cube \mathbf{X} is often represented as $\mathbf{X} := [\mathbf{x}_{l,n}]_{l,n}$, where $\mathbf{x}_{l,n} \in \mathbb{R}^E$ is the (l, n) -th element of the data cube, representing the RF data measured by the receiver channels from the l -th scan line at the depth index n . The time-delay corrected data cube $\mathbf{Y} \in \mathbb{R}^{L \times N \times E}$ is similarly denoted by $\mathbf{Y} = [\mathbf{y}_{l,n}]_{l,n}$, where

$$\mathbf{y}_{l,n} = [y_{l,n}[0] \quad y_{l,n}[1] \quad \cdots \quad y_{l,n}[E-1]]^\top \in \mathbb{R}^E \quad (1)$$

with

$$y_{l,n}[i] := x_{l,n}[i - \tau_{l,n}[i]].$$

Here, $\tau_{l,n}[i]$ is the time delay for the i -th receiver elements to obtain the l -th scan line at the depth n .

In many US imaging, only a subset of receiver channels are used to process return echoes to save power consumption and/or data rate. Usually, the aperture, which refers to the span of the active receiver, varies depending on the scan lines, so that symmetric set of receivers along the scan lines are used. In this case, the received RF data can be explicitly modeled as $\mathbf{Z} = [\mathbf{z}_{l,n}]_{l,n}$, where

$$\mathbf{z}_{l,n} = [z_{l,n}[0] \quad z_{l,n}[1] \quad \cdots \quad z_{l,n}[E-1]]^\top \in \mathbb{R}^C \quad (2)$$

and

$$z_{l,n}[i] = y_{l,n}[i + d_l] \quad (3)$$

where d_l denotes the specific detector offset to indicate the active channel elements, which is determined for each scan line index l . See Fig. 1(a) for the conversion between the data cube \mathbf{X} and \mathbf{Z} , where the dark triangular regions in \mathbf{X} , which correspond to inactive receiver elements, are removed in constructing \mathbf{Z} .

B. Classical Beamforming

1) *DAS beamforming*: The standard delay and sum (DAS) beamformer for the l -th scanline at the depth sample n can be expressed as

$$u_{l,n} = \frac{1}{J} \mathbf{1}^\top \mathbf{z}_{l,n}, \quad l = 0, \dots, L-1, \quad (4)$$

where \top denotes the transpose, $\mathbf{1}$ denotes a C -dimensional column-vector of ones and J is the number of active channel (i.e. aperture size).

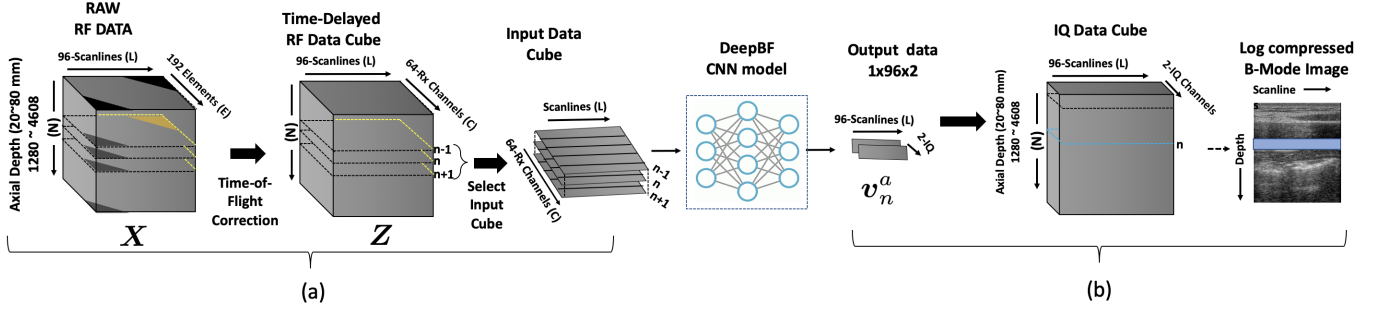


Fig. 1. Our deep beamformer pipeline. The highlighted region in B-mode image is the output generated by the neural network for given input RF data.

2) *Adaptive beamforming*: The DAS beamformer is designed to extract the low-frequency spatial content that corresponds to the energy within the main lobe; thus, it is difficult to control side lobe leakage. Reduced side lobe leakage can be achieved by replacing the uniform weights by tapered weights:

$$w_{l,n} = \mathbf{w}_{l,n}^\top z_{l,n}, \quad (5)$$

where $\mathbf{w}_{l,n} \in \mathbb{R}^C$. Specifically, in adaptive beamforming the objective is to find the $\mathbf{w}_{l,n}$ that minimizes the variance of $w_{l,n}$, subject to the constraint that the gain in the desired beam direction equals unity. For example, the minimum variance (MV) estimation task can be formulated as [2]–[4]

$$\begin{aligned} \underset{\mathbf{w}_{l,n}}{\text{minimize}} \quad & E[|w_{l,n}|^2] = \min_{\mathbf{w}_{l,n}} \mathbf{w}_{l,n}^\top \mathbf{R}_{l,n} \mathbf{w}_{l,n} \\ \text{subject to} \quad & \mathbf{1}^\top \mathbf{w}_{l,n} = 1, \end{aligned}$$

where $E[\cdot]$ is the expectation operator over RF data distribution, and $\mathbf{R}_{l,n}$ is a spatial covariance matrix given by:

$$\mathbf{R}_{l,n} = E[z_{l,n} z_{l,n}^\top]. \quad (6)$$

Then, $\mathbf{w}_{l,n}$ can be obtained by Lagrange multiplier method [39] and expressed as

$$\mathbf{w}_{l,n} = \frac{\mathbf{R}_{l,n}^{-1} \mathbf{1}}{\mathbf{1}^\top \mathbf{R}_{l,n}^{-1} \mathbf{1}}. \quad (7)$$

C. Deconvolution Ultrasound

One of the main limitations of the aforementioned beamforming methods is that they are based on the ray approximation of the wave propagation, whereas the real sound propagation exhibits many wave phenomenon such as scattering, etc. Moreover, the precision of the time delay $\tau_{l,n}[i]$ calculation is determined by bandwidth of the transducers, which limits the accuracy of delayed signal $y_{l,n}[i] := x_{l,n}[i - \tau_{l,n}[i]]$. These modeling inaccuracy may affect the spatial resolution and the contrast of standard US images.

In order to overcome these issues, many researchers have explored the deconvolution of US images [40], [41]. Specifically, the deconvolution US tries to find the filter kernel $h_{l,n}$ such that the filtered signal $v_{l,n}$ given by

$$v_{l,n} = (h * u)_{l,n} \quad (8)$$

produces high resolution images.

D. Imposing Causality Condition

Another important step after the beamforming is to convert the processed data to a causal signal using Kramers–Kronig relation [42]. This step is necessary to detect the signal envelope. More specifically, this process is performed by

$$v_{l,n}^a = v_{l,n} + \iota(\kappa * v)_{l,n} = ((\delta + \iota\kappa) * v)_{l,n}, \quad (9)$$

where $\iota = \sqrt{-1}$, and δ is a discrete Dirac delta function, and κ denotes the filter kernel for Hilbert transform. The filter kernel for Hilbert transform is in principle one-dimensional since it is applied along the depth direction. Here, $v_l^a[n]$ is often referred to as the in-phase (I) and quadrature (Q) representation.

E. Putting Together

By using (5), (8) and (9), we can obtain the following representation:

$$v_{l,n}^a = ((h + \iota\kappa * h) * u)_{l,n} \quad (10)$$

If we define

$$\mathbf{v}^a = \begin{bmatrix} v_0^a \\ \vdots \\ v_{N-1}^a \end{bmatrix}, \quad \text{where} \quad \mathbf{v}_n^a = \begin{bmatrix} v_{0,n}^a \\ \vdots \\ v_{L-1,n}^a \end{bmatrix} \quad (11)$$

and

$$\mathbf{z} = \begin{bmatrix} z_0 \\ \vdots \\ z_{N-1} \end{bmatrix}, \quad \text{where} \quad \mathbf{z}_n = \begin{bmatrix} z_{0,n} \\ \vdots \\ z_{L-1,n} \end{bmatrix} \quad (12)$$

then the following matrix representation can be obtained:

$$\mathbf{v}^a = \tilde{\mathbf{B}} \mathbf{u} \quad (13)$$

where $\tilde{\mathbf{B}}$ is a 2-D convolution matrix composed of the filter kernel $h + \iota\kappa * h$, and

$$\mathbf{u} := \mathbf{B}(\mathbf{z})\mathbf{z}, \quad \text{where} \quad \mathbf{B}(\mathbf{z}) = \mathbf{I} \otimes \mathbf{W}(\mathbf{z})^\top$$

where \otimes is a Kronecker product and $\mathbf{W}(\mathbf{z})$ is the input-dependent beamformer adaptive weight matrix given by

$$\mathbf{W}(\mathbf{z}) := [\mathbf{w}_{0,0} \quad \cdots \quad \mathbf{w}_{L-1,0} \quad \cdots \quad \mathbf{w}_{L-1,N-1}]$$

Accordingly, Eq. (13) can be equivalently represented as a nonlinear mapping:

$$\mathbf{v}^a = \mathcal{T}(\mathbf{z})\mathbf{z} \quad (14)$$

where $\mathcal{T}(z) := \tilde{\mathbf{B}}\mathbf{B}(z)$. Then, the goal of the US reconstruction is to find the nonlinear mapping $\mathcal{T}(z)$ so that the processed image has a high resolution with good contrast and better signal-to-noise ratio.

III. MAIN CONTRIBUTION

A. Piecewise linear approximation using CNN

In practice, the estimation of $\mathcal{T}(z)$ in (14) is technically challenging. This is because the beamformer weights are dependent on each RF data z . Moreover, the deconvolution filter matrix could be also spatially varying. Therefore, the exact calculation is usually computationally expensive. A quick remedy to overcome this would be precalculating nonlinear mapping $\mathcal{T}(z)$. Unfortunately, it requires huge memory to store $\mathcal{T}(z)$ for all z .

In this regard, a convolutional neural network (CNN) using ReLU nonlinearities provides an ingenious way of addressing this issue. Specifically, in our recent theoretical work [36], we have shown that an encoder-decoder CNN with ReLU nonlinearity generates large number of distinct linear mappings depending on inputs. More specifically, the input space is partitioned into non-overlapping regions where input for each region share a common linear representation or mapping. [36].

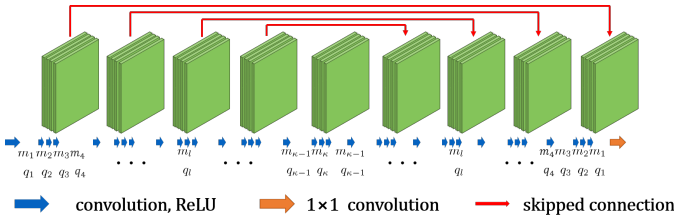


Fig. 2. Encoder-decoder CNN backbone.

Specifically, consider an encoder-decoder CNN with the output v^a with respect to input z as shown in Fig. 2, where there exists skipped connection for every four convolution operations. As shown in Appendix, the output v^a of the encoder-decoder CNN with respect to input z can be represented by the following nonlinear mapping:

$$v^a = \mathcal{T}_{\Theta}(z)z = \sum_i \langle b_i(z), z \rangle \tilde{b}_i(z) \quad (15)$$

where Θ refers to all the convolution filter parameters, and $b_i(z)$ and $\tilde{b}_i(z)$ denote the i -th column of the matrices (A.8) and (A.9), respectively.

The expression (A.7) reveals many important aspects of neural networks. First, the CNN representation in (A.7) has explicit dependency on the input z in (A.7), due to the input dependent ReLU activation pattern. Accordingly, even from the same filter set, the input-dependent ReLU activation pattern makes the resulting mapping vary depending on the input signals. Furthermore, the number of distinct linear representation increases exponentially with the number of neurons determined by network depth and width [36], since the distinct ReLU activation pattern is in principle combinatorially many up to $2^{\# \text{ of neurons}}$. Second, the number of blocks in $\mathbf{B}(z)$ and $\tilde{\mathbf{B}}(z)$ in (A.8) and (A.9) are determined by the number

of skipped connections, so the skipped branch makes the representation more redundant, which again makes the neural network have more piecewise linear regions [36].

Note that the piecewise linear representation using (15) is useful for approximating our nonlinear mapping $\mathcal{T}(z)$ in (14). Specifically, the piecewise linear representation by the DeepBF can be obtained by learning the filters Θ from the following optimization problem:

$$\min_{\Theta} \sum_{t=1}^T \|v^{a(t)} - \mathcal{T}_{\Theta} z^{(t)}\|_2^2, \quad (16)$$

where $\{(z^{(t)}, v^{a(t)})\}_{t=1}^T$ denotes the training data set composed of RF data and the target IQ data, which are collected across all subjects and subsampling patterns. Although the piecewise linear property of CNN may appear as a limitation to approximate arbitrary nonlinear functions, it also provides good architectural prior known as *inductive bias*, which results in inherent regularization effects. As will be shown in experimental results, we found that this inductive bias works favorable for US reconstruction.

B. Proposed Deep Beamformer Pipeline

One of the limitations of the original training framework in (16) is that the RF data input z and the target v^a requires too big memory to store using GPU memory. Therefore, rather than training a neural network to learn the mapping between all RF data, we implemented a separable form of a neural network such that the neural network is trained to estimate one depth at a time. Specifically, with a slight abuse of notation, our neural network is designed as

$$v_n^a = \mathcal{T}_{\Theta}(s_n) s_n, \quad (17)$$

where s_n is a sub-set of input RF data z collected from three depth planes around the depth n :

$$s_n = [z_{n-1}^T \quad z_n^T \quad z_{n+1}^T]^T$$

where v_n^a and z_n are defined in (11) and (12), respectively. Then, the resulting neural network training is given by

$$\min_{\Theta} \sum_{t=1}^T \sum_{n=1}^N \|v_n^{a(t)} - \mathcal{T}_{\Theta} s_n^{(t)}\|_2^2, \quad (18)$$

where $\{(s_n^{(t)}, v_n^{a(t)})\}_{n,t=1}^{N,T}$ denotes the training data set collected across all depth planes. One of the potential limitations of using the restricted architecture (17) is the reduction of the depth-dependent adaptivity of the neural network, since all the depth information is used together as a target data. This issue will be revisited in experimental section.

Fig. 1 illustrates the proposed DeepBF pipeline using the reflected sound waves in the medium measured by the transducer elements. As a preprocessing for DeepBF pipeline, each measured RF signal \mathbf{X} is time-delayed to generate focused RF data cube \mathbf{Z} based on the traveled distance. Then, our DeepBF generates IQ data v^a directly from the time delayed RF data. Compared to the standard DAS beamformer, this corresponds to the replacement of the deconvolution, beamforming and Hilbert transform parts with a deep neural network. Then, the

signal envelope is generated by calculating the sum of squares of the in-phase and quadrature phase signals generated from the Hilbert transform. Finally, log compression is applied to generate the B-mode images.

IV. METHOD

A. Dataset

For experimental verification, we used an E-CUBE 12R US system (Alpinion Co., Korea). For data acquisition, we used a linear array transducer (L3-12H), whose configuration is given in Table I. Specifically, using the linear probe with a center frequency of 8.5 MHz, we acquired RF data from the carotid/thyroid area of 10 volunteers using focused B-mode US imaging. The *in vivo* data consist of 40 temporal frames per subject, providing 400 sets of TE-Depth-Rx data cube \mathbf{X} . In addition, we acquired 218 frames of RF data from the ATS-539 multipurpose tissue mimicking phantom using 8.5 MHz center frequency. The phantom dataset was only used for test purposes and no additional training of CNN was performed on it. In addition to the carotid/thyroid and phantom datasets we also acquired additional dataset from forearm and calf muscles. In particular, they were acquired using 10 MHz carrier frequency and consist of 100 frames 50 from each body part. This data set were used to further validate the generalization power of our trained model.

For all scans the axial depth was in the range of 20~80 mm, while lateral length was 38.4mm. Depending on the object of interest, the focal depth is adjust accordingly, in particular it varies in the range of 10~40 mm.

TABLE I
PROBE CONFIGURATION

Parameter	Linear Probe
Probe Model No.	L3-12H
Carrier wave frequency	8.5/10.0 MHz
Sampling frequency	40 MHz
Scan wave mode	Focused
No. of probe elements	192
No. of Tx elements	128
No. of TE events	96
No. of Rx elements	64 (from center of Tx)
Elements pitch	0.2 mm
Elements width	0.14 mm
Elevating length	4.5 mm

B. Network specification

Fig. 2 illustrates the schematic diagram of our deep beamformer. One minor improvement is the channel augmentation at the skipped branch of the decoder rather than simple addition. Moreover, to make the neural network process only real-valued data, the real and image components of v^a are separately processed to generate two channel IQ output.

The proposed CNN consists of 37 convolution layers (i.e. $\kappa = 4$) composed of a contracting path with concatenation, batch normalization, and ReLUs except for the last convolution layer. The first 36 convolution layers as shown in Fig. 2 use 3×3 convolutional filters (i.e., the 2-D filter has a dimension of 3×3), and the last convolution layer uses a 3×1 filter

followed by an average pooling to contract the $3 \times 96 \times 64$ data-cube from Depth-TE-Rx sub-space to $1 \times 96 \times 2$ Depth-TE-IQ plane. The number of CNN filter channel for each layer is $q_l = 64$ and the dimension of the signal is $m_l = 64 \times 96$ up to the last layer which shrinks it to $1 \times 96 \times 2$ Depth-TE-IQ data.

C. RF data sampling scheme

The input and output data configurations are shown in Fig. 1 (a) and (b) respectively. The time-delayed RF data cube \mathbf{Y} is a three-dimensional data cube composed of total 1280 ~ 4608 depths of 96×64 data in TE-Rx direction. We trained our neural network using multiple input/output pairs, where an input consists of $3 \times 96 \times 64$ data-cube in the Depth-TE-Rx volume and the output is composed of 96 pairs of I/Q data in the Depth-TE plane. Each target IQ pair corresponds to two output channels, each representing real and imaginary parts. A set of 30,000 Depth-TE-Rx cubes of size $3 \times 96 \times 64$ were randomly selected from 10 frames of four different subject's datasets, which are divided into 25,000 samples for training and 5,000 samples for validation. The remaining dataset of 360 frames was used as a test dataset.

For our experiments, in addition to the full RF data with 64 RF-channels, we generated five sets of sub-sampled RF data at different down-sampling rates. More specifically, the subsampling cases included 32, 24, 16, 8 and 4 Rx-channels at two subsampling schemes, such as variable down-sampling patterns across the depth and fixed down-sampling patterns across the depth. Since the active receivers at the center of the scan line get RF data from direct reflection, the two channels in the center were always included, the remaining channels are randomly selected from the other 62 active receiving channels and unselected Rx channels are zero-padded. In variable sampling scheme, different sampling pattern (mask) is used for each depth plane, whereas in fixed sampling we used same sampling pattern (mask) for all depth planes. The network was trained for variable sampling scheme only and both sampling schemes were used in test phase. The variable sub-sampling patterns can be implemented using a software changes by randomly selecting the A/D converter, of which procedure is similar to various compressive US researches, e.g. [11].

D. Network training

As for the target IQ data, we mainly used the IQ data from DAS beamforming results from the full RF data. We also use IQ data from an adaptive beamformer and deconvolution beamformer [43] to demonstrate that the proposed beamformer can be trained to mimic various types of beamformers.

The network was implemented with MatConvNet [44] in the MATLAB 2015b environment. Specifically, for network training, the parameters were estimated by minimizing the l_2 norm loss function using a stochastic gradient descent with a l_2 regularization parameter of 10^{-4} . The learning rate started from 10^{-4} and exponentially decreased to 10^{-7} in 200 epochs. The weights were initialized using Gaussian random distribution with the Xavier method [45].

It is noteworthy to highlight this important aspect of our DeepBF model that a single (one time trained) CNN model is used for all data types and sub-sampling rates.

E. Comparison methods

For the evaluation purpose, we compared our proposed DeepBF method with standard DAS and MV beamformers. In DAS, the beamforming step is a simple weighted sum. Specifically, for DAS formulation in (4), J is varied from 64 to 4 depending on the sub-sampling ratios so that data from J active receivers is added to generate beamformed output. For the adaptive beamforming case, $\mathbf{R}_{l,n}$ must be estimated with a limited amount of data. A widely used method for the estimation of $\mathbf{R}_{l,n}$ is spatial smoothing (or subaperture averaging) [46], in which the sample sub-aperture covariance matrix is calculated by averaging covariance matrices of K consecutive channels in the J receiving channels. Here we use $K = 16$. Then, the weight for the minimum variance beamformer is calculated using the sub-aperture covariance estimate, after which the final beamforming result is obtained by averaging the contribution from the adaptive beamforming results from each subaperture array.

F. Performance metrics

To quantitatively show the advantages of the proposed deep learning method, we used the contrast-recovery (CR), contrast-to-noise ratio (CNR) [47], generalized CNR (GCNR) [48], peak-signal-to-noise ratio (PSNR), structure similarity (SSIM) [49] and the reconstruction time.

The contrast is measured for the background (B) and anechoic structure (aS) in the image, and quantified in terms of CR and CNR:

$$\text{CR}(B, aS) = |\mu_B - \mu_{aS}| \quad (19)$$

$$\text{CNR}(B, aS) = \frac{|\mu_B - \mu_{aS}|}{\sqrt{\sigma_B^2 + \sigma_{aS}^2}}, \quad (20)$$

where μ_B , μ_{aS} , and σ_B , σ_{aS} are the local means, and the standard deviations of the background (B) and anechoic structure (aS) [47], respectively. Another improved measure for the contrast-to-noise-ratio called generalized-CNR (GCNR) was recently proposed [48]. The GCNR compare the overlap between the intensity distributions of two regions. The GCNR is defined as

$$\text{GCNR}(B, aS) = 1 - \int \min\{p_B(x), p_{aS}(x)\} dx, \quad (21)$$

where x is the pixel intensity, and p_B and p_{aS} are the probability distributions of the background (B) and anechoic structure (aS), respectively. If both distribution are completely independent, then GCNR will be equals to one, whereas, if they completely overlap then GCNR will be zero [48]. The GCNR measure is difficult to tweak, so we believe that GCNR is an objective performance metric. For CNR and GCNR calculations, we generated separate ROI masks for each image.

The PSNR and SSIM index are calculated on reference (v) and Rx sub-sampled (\tilde{v}) images of common size $n_1 \times n_2$ as

$$\text{PSNR}(v, \tilde{v}) = 10 \log_{10} \left(\frac{R_{\max}^2}{\|v - \tilde{v}\|_F^2} \right), \quad (22)$$

where $\|\cdot\|_F$ denotes the Frobenius norm and $R_{\max} = 2^{(\#\text{bits per pixel})} - 1$ is the dynamic range of pixel values (in our experiments this is equal to 255), and

$$\text{SSIM}(v, \tilde{v}) = \frac{(2\mu_v\mu_{\tilde{v}} + c_1)(2\sigma_{v,\tilde{v}} + c_2)}{(\mu_v^2 + \mu_{\tilde{v}}^2 + c_1)(\sigma_v^2 + \sigma_{\tilde{v}}^2 + c_2)}, \quad (23)$$

where μ_v , $\mu_{\tilde{v}}$, σ_v , $\sigma_{\tilde{v}}$, and $\sigma_{v,\tilde{v}}$ are the local means, standard deviations, and across-covariance for images v and \tilde{v} calculated for a radius of 50 units. The default values of $c_1 = (k_1 R_{\max})^2$, $c_2 = (k_2 R_{\max})^2$, $k_1 = 0.01$ and $k_2 = 0.03$.

V. EXPERIMENTAL RESULTS

In this section we present extensive comparison results of our method with DAS and the minimum variance beamformer (MVBF) for various acquisition scenarios. Our DeepBF was first trained with DAS data obtained from full RF data, and we compare our results with those by DAS and the minimum variance beamformer (MVBF). We also trained our neural network using the MVBF from full RF data. With a slight abuse of terminology, this is often referred to as DeepMVBF, although we use the term DeepBF to refer general deep neural network-based beamformers regardless of specific target data for training.

A. Quantitative comparison

We compared the CR, CNR, GCNR, PSNR, and SSIM distributions of reconstructed B-mode images of *in vivo* and phantom test datasets. Table II shows the comparison of DAS, MVBF, proposed DeepBF, and DeepMVBF methods on 360 *in vivo* test frames for random sub-sampling scheme. In terms of CR, CNR and GCNR, the overall performance of DAS and MVBF were relatively similar. However, the results by the proposed methods are significantly superior to those of DAS and MVBF at various subsampling factors. To investigate the performance degradation with respect to the subsampling, in Table II we also show the PSNR and SSIM values with respect to the results of the full scan. Again, the performance degradation in terms of PSNR and SSIM was much less by the proposed DeepBF and DeepMVBF.

In Fig. 3, we provides distribution plots for various performance measures for phantom test dataset. In fully sampled case, our DeepBF shows overall gain of around 1.23 dB in CR, and 0.07 units improvement in CNR compared to DAS. In sub-sampling cases, unlike DAS and MVBF in which the performance is highly sensitive to the rate of sub-sampling, the proposed DeepBF shows consistent GCNR performance even at $4\times$ reduced sampling rate. This can be easily seen in Fig. 3 (third row), where the average value of GCNR remain constant at 0.90 units for $1\times$ to $4\times$ sampling factors and only drop by 0.03 and 0.04 units at $8\times$ and $16\times$ sampling factors respectively. The performance of DeepBF and DeepMVBF were similar, although DeepMVBF has slight better CR values.

TABLE II
PERFORMANCE STATISTICS ON *in vivo* DATA FOR RANDOM SAMPLING PATTERN

sub-sampling factor	CR (dB)				CNR				GCNR				PSNR (dB)				SSIM			
	DAS	MVBF	DeepBF	DeepMVBF	DAS	MVBF	DeepBF	DeepMVBF	DAS	MVBF	DeepBF	DeepMVBF	DAS	MVBF	DeepBF	DeepMVBF	DAS	MVBF	DeepBF	DeepMVBF
1	12.37	12.39	13.25	13.25	1.38	1.38	1.45	1.45	0.64	0.64	0.66	0.66	∞	∞	∞	∞	1	1	1	1
2	10.55	10.62	13.05	13.26	1.33	1.33	1.47	1.47	0.63	0.63	0.66	0.66	24.59	24.63	27.38	27.71	0.89	0.89	0.95	0.95
2.7	10.06	10.16	12.63	13.29	1.30	1.30	1.44	1.48	0.62	0.62	0.66	0.67	23.15	23.17	25.54	26.08	0.86	0.86	0.92	0.93
4	9.54	9.65	11.80	13.14	1.25	1.25	1.38	1.47	0.60	0.60	0.65	0.66	21.68	21.75	23.55	24.29	0.81	0.81	0.87	0.89
8	9.05	9.21	10.47	12.17	1.18	1.19	1.26	1.37	0.58	0.58	0.61	0.64	19.99	20.02	21.03	21.96	0.74	0.74	0.78	0.82
16	8.98	9.11	9.73	10.99	1.12	1.11	1.17	1.25	0.56	0.56	0.58	0.61	18.64	18.68	19.22	20.24	0.67	0.67	0.69	0.74

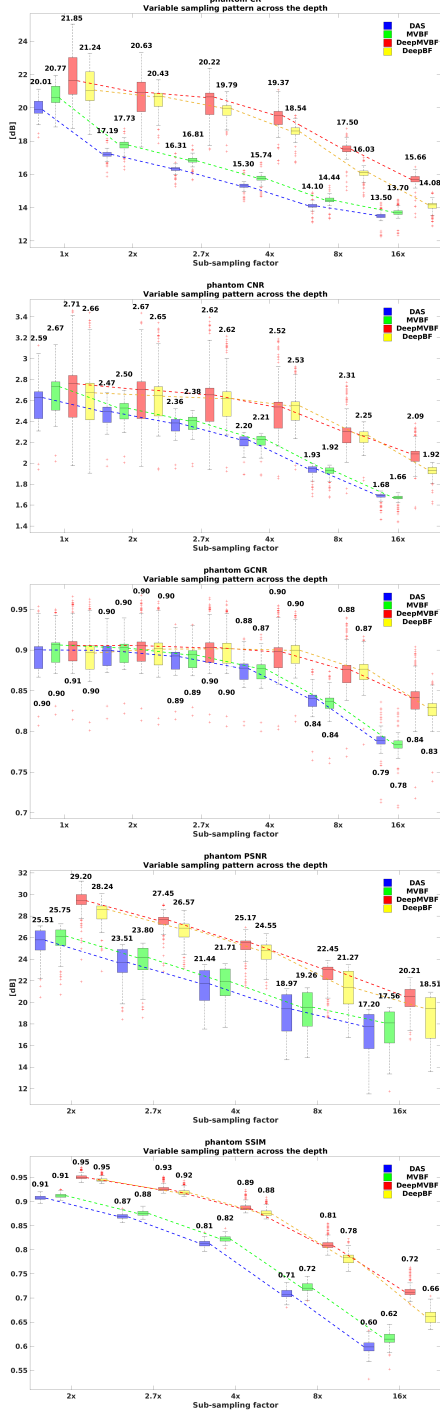


Fig. 3. Quantitative comparison using phantom data with respect to different subsampling rate: (first row) CR value distribution, (second row) CNR value distribution, (third row) GCNR value distribution, (fourth row) PSNR value distribution, (fifth row) SSIM value distribution

The CR, CNR, and GCNR are the measure for local regions, whereas the PSNR and SSIM are the global metric. To calculate the PSNR and SSIM, images generated using 64 Rx-channels were considered as reference images for all algorithms. As shown in Fig. 3 the proposed methods show significantly higher PSNR and SSIM values, confirming that the proposed methods successfully recover actual structural detail in sub-sampled images.

B. Qualitative Comparison

To verify the performance improvement in terms of visual quality, here we provide representative reconstruction results. Due to the similarity between the DeepBF and DeepMVBF, we only provide the results by DeepBF in this section.

1) *Full RF data cases*: In Fig. 4 we compared two phantom examples scanned using 8.5 MHz center frequency. In phantom test dataset, the proposed DeepBF achieves comparable or even better performance compared to DAS and MVBF methods. From the figures we found that the visual quality of DeepBF reconstruction, especially around anechoic regions, is comparable or better than that of MVBF method, which is better than DAS beamformer. Quantitatively, CR, CNR, and GCNR values of Deep BF were slightly improved compared to the existing methods. It is also noteworthy to point-out that even though the proposed DeepBF was only trained on *in vivo* carotid/thyroid data scanned with 8.5MHz operating frequency, its performance in very diverse test scenarios is still remarkable, which clearly shows the generalization power of the proposed method.

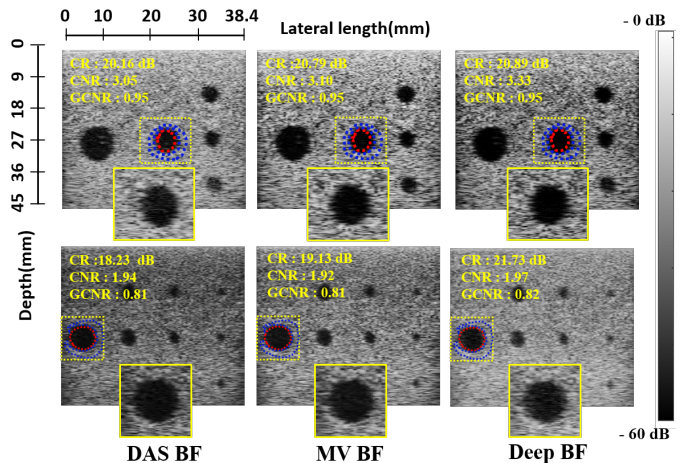


Fig. 4. Reconstruction results of standard DAS BF, MV BF and the proposed DeepBF for fully sampled phantom scans data using 8.5 MHz center frequency.

To further validate the performance gain on fully-sampled data, in Fig. 5 we showed the results of two *in vivo* examples for fully-sampled data. The images are generated using standard DAS, MVBF and the proposed DeepBF method. In Fig. 5, it can be easily seen that our method provides visual quality comparable to DAS and MVBF methods. Interestingly, it is remarkable that the CR, CNR and GCNR values are improved by the DeepBF. To investigate the origin of the quantitative improvement, we showed the magnified views as inset in Fig. 5. With a careful look, we can see that there are several artifacts around the wall of anechoic regions in DAS and MVBF methods, which can be confused with structure. On the other hand, those artifacts are not visible in DeepBF, which makes the the visual quality of the US images and quantitative values higher compared to DAS and MVBF methods.

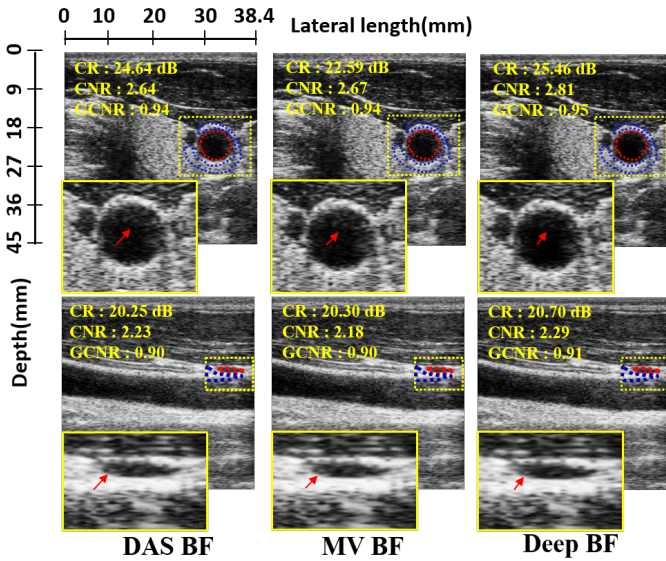


Fig. 5. Reconstruction results of standard DAS-BF, MVBF and the proposed DeepBF for fully sampled *in vivo* scans from Carotid region. All the figures are illustrated at the same window level (0 ~ -60dB for the beamformed images).

2) *Compressive beamforming*: Fig. 6 show the results of a phantom example for 32, 16, and 4 Rx-channels down-sampling schemes on random sampling scheme. Since 64 channels are used as a full sampled data, this corresponds to the full data as well as subsampled data with $2\times$, $4\times$ and $16\times$ sub-sampling factors. The images are generated using the proposed DeepBF, MVBF and the standard DAS beamformer methods. Our method significantly improves the visual quality of the US images by estimating the correct structural details and eliminating artifacts caused by sub-sampling. The residual of fully-sampled and sub-sampled images are shown in pseudo colors on normalized scale. From the normalized difference images it can be easily seen that DeepBF produces uniformly distributed noise-like errors across various subsampling ratios, whereas DAS and MVBF produce structure-dependent errors that can reduce the image contrast. Note that the training data consist of only *in vivo* carotid/thyroid scans; but relative improvement in diverse test scenarios is nearly the same for

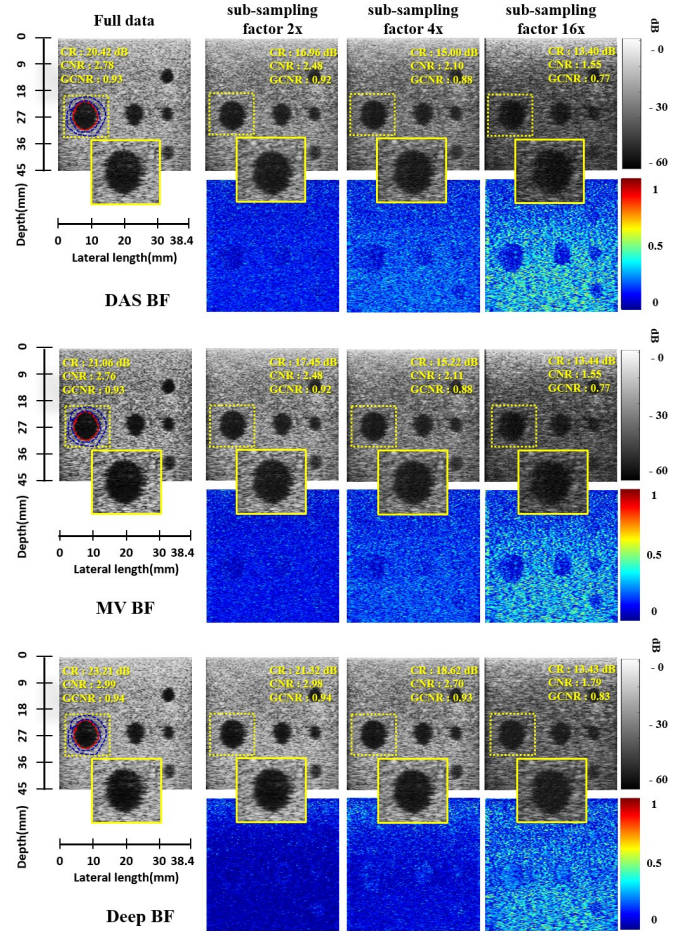


Fig. 6. Comparison of various beamformers for phantom data with random sub-sampling patterns. The difference image is normalized to 0 ~ 1 scale for each image.

both *in vivo* and phantom cases. This further confirms the generalization power of the proposed method.

Fig. 7 illustrates representative examples of *in vivo* data at 2 ~ 16x acceleration. By harnessing the spatio-temporal (multi-depth and multi-line) learning, the proposed CNN-based beam-former successfully reconstructs the images with good quality in all down-sampling schemes. From residual images it can be seen that in contrast to DAS and MVBF, the proposed DeepBF maintains good visual quality at even at highest sub-sampling rate. Unlike DAS and MVBF, DeepBF preserves the original structural details as well as the contrast of the sub-sampled data much closer to the fully-sampled image.

C. Computational time

One big advantage of ultrasound image modality is its runtime imaging capability, which requires fast reconstruction time. Although training required 40 hours for 200 epochs using MATLAB, once training was completed, the reconstruction time for the proposed deep learning method is not very long. The average reconstruction time for each depth plane is around 4.8 (milliseconds), which could be easily reduced

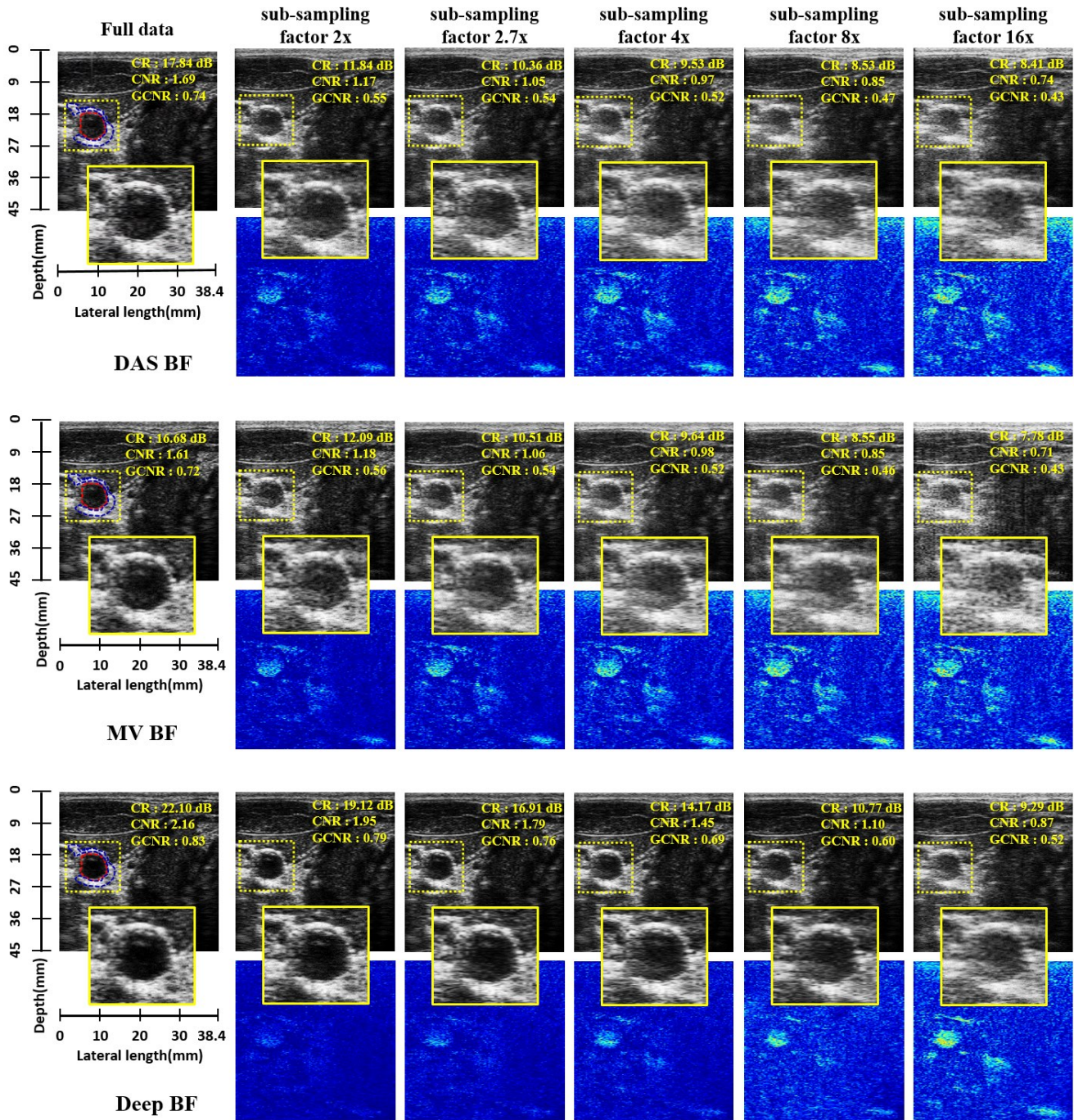


Fig. 7. Comparison of various beamformers for in vivo data with random sub-sampling patterns. The images are shown in the same window level ($0 \sim -60$ dB for the beamformed images, and the difference image is normalized to $0 \sim 1$ scale for each image.)

by optimized implementation and reconstruction of multiple depth planes in parallel.

VI. DISCUSSION

A. Expressivity and Generalization

To confirm that the proposed neural network learns various target data, we also trained our model using deconvolution of DAS results. The training was performed using fine-tuning method using target data generated by a deconvolution method using sparse representation as described in [43]. In Fig 8, we

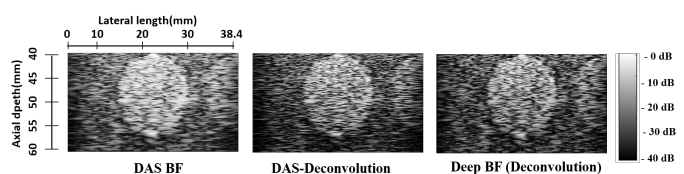


Fig. 8. Comparison of DAS, deconvolution of DAS, and proposed DeepBF with deconvoluted DAS as label using phantom anechoic cyst of 15 mm diameter at 40 mm depth on fully sampled RF-data.

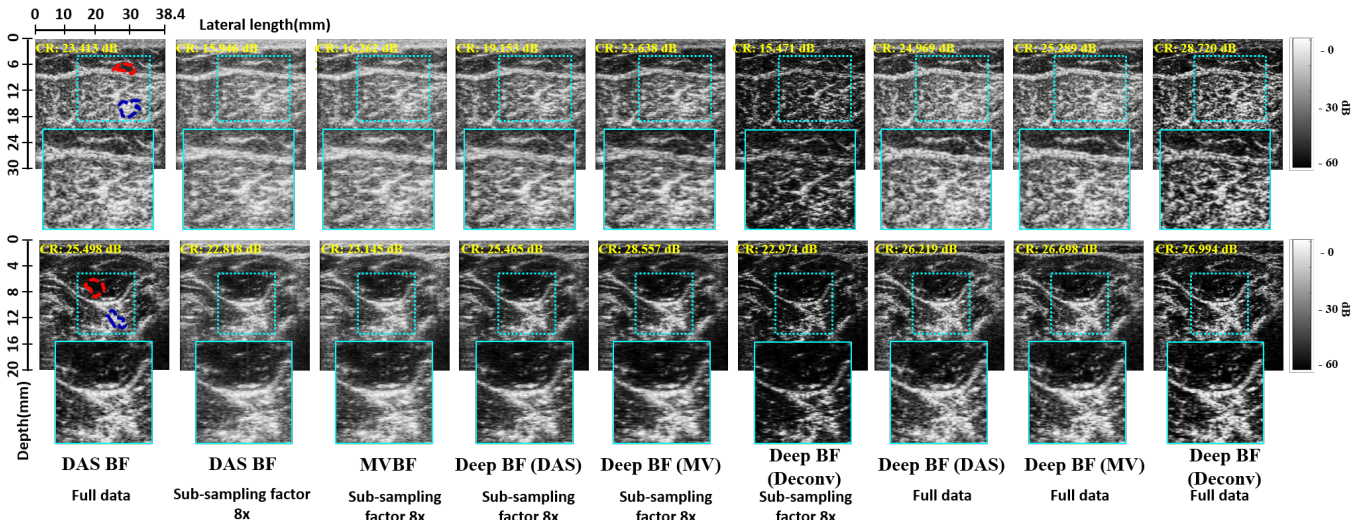


Fig. 9. Reconstruction results from (left) forearm muscle (right) calf muscle using standard DAS, MVBF, and Deep BFs at various random subsampling factors. Here, various form of Deep BF were trained using DAS, MVBF, and deconvoluted DAS as target data from fully sampled *in vivo* scans. All the figures are illustrated at the same window level (0 ~ -60dB for the beamformed images).

compared the reconstruction results by DAS, deconvolution of DAS, and the proposed DeepBF trained with deconvoluted DAS as target, using phantom anechoic cyst of 15 mm diameter at 40 mm depth on fully sampled RF-data. From the results it can be easily seen that the proposed method can successfully learn to mimic the deconvolution method.

To further compare the effect of various choices of target data and its generalization power, we evaluated the network trained with different label data by testing on completely different dataset. Specifically, we trained our neural network using fully sampled DAS images, MVBF images, and deconvolution results. Then, new test dataset were acquired from forearm and calf muscles using 10MHz carrier frequency. In Fig 9, it is evident that the proposed DeepBF method can successfully process RF-data from different anatomical region and operating frequencies. Among the various choices of the target data, the performance using the deconvoluted DAS target was best with less clutters, which was followed by DeepBF trained using MVBF targets and DAS targets. It is also noteworthy to point out that neural network trained with DAS targets still provides better results than the standard DAS and MVBF for x8 subsampling cases. In particular, on average DAS and MVBF showed 21.11 dB and 21.38 dB CR which is 2.06 dB and 1.79 dB less than the DeepBF respectively. Moreover, the performance of DeepBF and DeepMVBF were again somewhat similar.

B. Dependency on the Sampling Patterns

So far we showed that a considerable reduction in data rate can be achieved by applying DeepBF method, leading to a sub-Nyquist sampling rate, which uses only a portion of the bandwidth of the ultrasound signals to reconstruct the high quality image. Another application of sub-sampled US is the reduction of active Rx elements. For this purpose we also evaluated our model using uniform sub-sampling scheme to confirm whether relative performance gain with uniform

sub-sampling is also similar to the random sub-sampling. In Table III we compared the performance of proposed DeepBF method with DAS and MVBF on *in-vivo* data for uniform sub-sampling pattern. We can see in uniform sub-sampling case DeepBF achieves relatively similar performance gain as in the case of random sub-sampling. In Fig 10 two visual examples are shown for *in-vivo* and phantom datas, and we found that the proposed method successfully reconstruct the uniformly sub-sampled RF-data in both cases with equal error rates.

C. Ablation Studies

We also compared our method with Deep RF interpolation method [31]. Again, the proposed method also outperform the Deep RF interpolation method [31]. Fig 11 shows reconstruction results of various methods at $4\times$ subsampling rate, which is compared with the full data reconstruction. The contrast of the DeepBF, especially at anechoic regions, are very close to the full sampled case, whereas the other methods generates artifacts like patterns. Quantitatively, for $4\times$ sub-sampled *in vivo* test dataset, the Deep RF interpolation [31] achieves CNR, GCNR, PSNR, and SSIM values of 1.31, 0.63 units, 22.15 dB and 0.82 units, which are 0.07, 0.02 units, 1.4 dB and 0.05 units inferior to the proposed method respectively. Here we would like to point out that, in [31], deep learning approach was designed for interpolating missing RF data, which are later used as input for standard beamformer. On the other hand, the proposed method is a CNN-based beamforming pipeline, without requiring additional beamformer. Consequently, this approach is much simpler and can be easily incorporated to replace the standard beamforming pipeline.

The proposed multi-line, multi-depth method is also compared with different design strategies which include (1) reconstruction of RF sum without Hilbert transform (RF-sum only), (2) reconstruction of IQ data after training on fixed sub-sampling ratios (fixed sampling), and reconstruction of IQ data using only single depth plane (single-depth). Specifically,

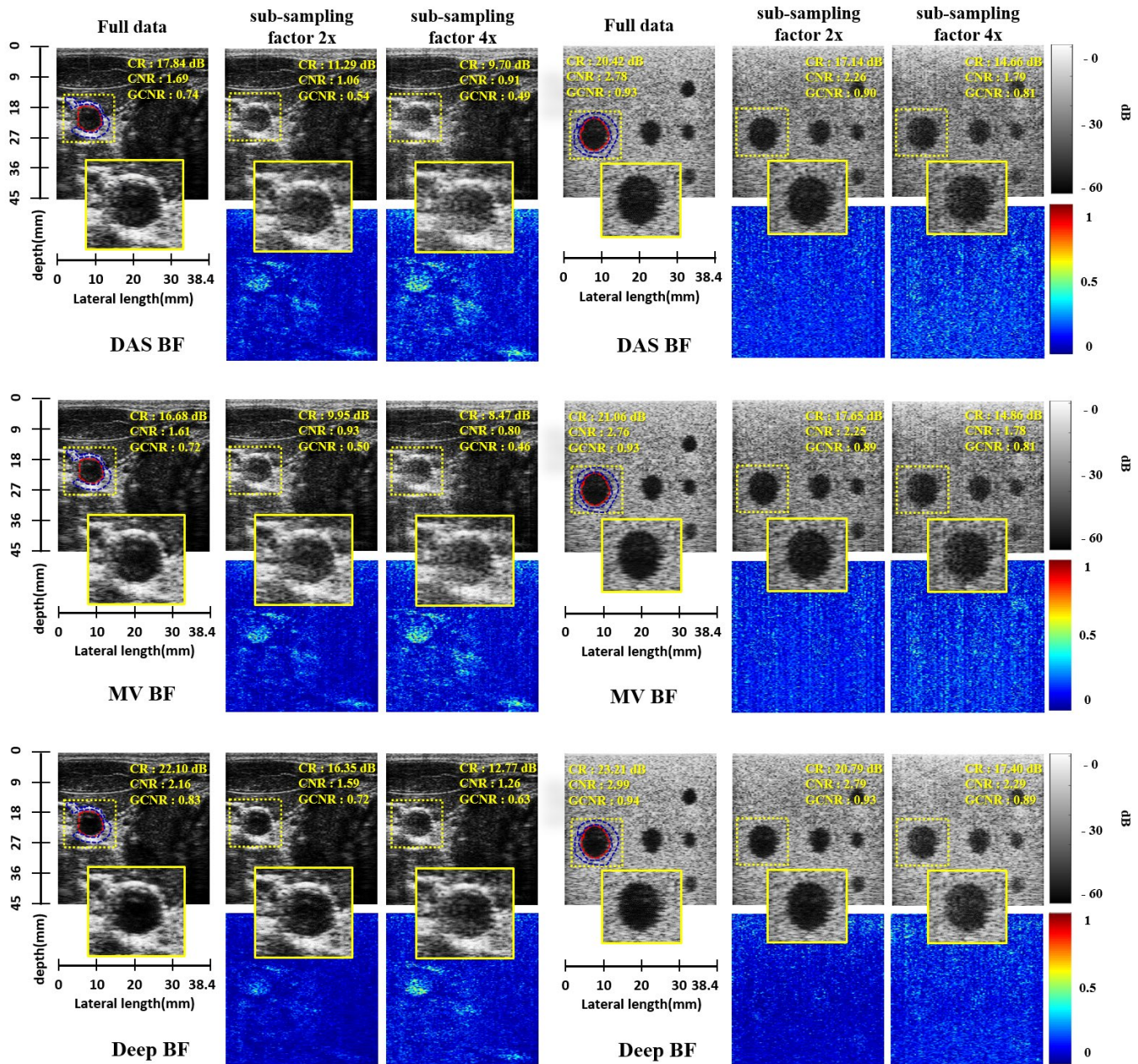


Fig. 10. Comparison of various beamformers for phantom data using uniform sub-sampling patterns. The difference image is normalized to 0 ~ 1 scale for each image.

Table IV compares the performance of different design choices on phantom data for random sub-sampling case. The results clearly show that the proposed methods of data-driven learning to generate IQ data using training data from multiple sub-sampling rates and multiple depths provides the best quantitative values. Especially at higher sampling rates the multi-depth method show high PSNR and SSIM measures. Although we just used 3 depth planes in this experiment, for further improvements the idea can be generalized to different number of depth planes.

D. Improved Lateral Resolution

In Fig 12, we compared lateral and axial profiles through the center of a phantom anechoic cyst using DAS, MVBF and proposed methods. In particular, an anechoic cysts of 6mm diameter scanned from the depth of 52mm and B-mode images were obtained for full data as well as random sampling with $2\times$ and $16\times$ sub-sampling factors using DAS, MVBF and proposed DeepBF methods. From the figures it can be seen that under all sampling schemes, on the boundary of cysts the proposed method show sharp changes in the pixel intensity with respect to the lateral position in the image. Although the axial profile shows similar trend to DAS for all subsampling rates, there are considerable gain in lateral resolution by the

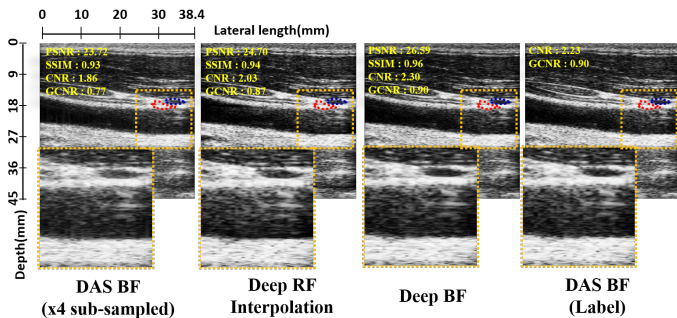


Fig. 11. Reconstruction results of standard DAS beam-former, Deep RF Interpolation [31] and the proposed DeepBF for $4\times$ sub-sampled in vivo data. The window levels are same for all images ($0 \sim -60$ dB).

proposed DeepBF compared to its DAS, MVBF counterparts. Again, similar qualitative performance improvement was seen using DeepBF and DeepMVBF, but the contrast enhancement was noticeable using the proposed methods with deconvoluted targets (DeepDeconv). This phenomenon was consistently observed for all sub-sampling factors.

We believe that this may be originated from the inherent synthetic aperture that are originated from our training that uses multiple scanlines, Rx, and depths as shown in (18). Recall that the input data s_n is composed of z_{n-1}, z_n, z_{n+1} which are composed of multiple scan line data as defined in (12). On the other hand, the resolution improvement along the axial directions was not significant, which may be due to depth-independent training scheme in (18), which may lose the depth-dependent adaptivity. The original training scheme in (16) may be a solution for this, but requires huge memory. The way to overcome this technical limitation is important, and will be investigated in other publications.

In spite of the memory reduction using (18), it still requires larger memory compared to the standard DAS, since it should store multiple scan line data. In our future work we will explore the possible solutions to design an end-to-end beam-former method using a single-scanline data, which can learn the time delay but still provides better performance than the classical beamformers. In addition, although the performance of the proposed deep learning approach is better than the classical beamformer, after $2.7\times$ sub-sampling factor, the proposed method still degrades the image quality. Additional strategy to improve the performance of the proposed method is still required, which is the another important research direction. Finally, the average reconstruction time of 4.8 (milliseconds) per depth is still slow for real time implementation. This is believed to be an engineering issue where optimized software implementation other than Matlab in addition to use of multiple GPUs may address the problem.

VII. CONCLUSION

In this paper, we presented a novel deep learning-based adaptive and compressive beamformer to generate high-quality B-mode ultrasound image. The proposed method is purely a data-driven method which exploits the spatio-temporal redundancies in the raw RF data, which help in generating improved

quality B-mode images using various transducer numbers. The proposed method can be trained using various targets, such as DAS, MVBF, and deconvoluted beamforming results from full RF data to satisfy the desired IQ for each application. The proposed method improved the contrast of B-modes images by preserving the dynamic range and structural details of the RF signal in both the phantom and *in vivo* scans. Therefore, this method can be an important platform for ultrasound imaging.

APPENDIX

Although this part is basically a summary of [36], we have included it to make the paper self-contained.

Consider encoder-decoder networks in Fig. 2. The network has symmetric configuration so that both encoder and decoder have the same number of layers, say κ ; the input and output dimensions for the encoder layer \mathcal{E}^l and the decoder layer \mathcal{D}^l are symmetric:

$$\mathcal{E}^l : \mathbb{R}^{d_{l-1}} \mapsto \mathbb{R}^{d_l}, \quad \mathcal{D}^l : \mathbb{R}^{d_l} \mapsto \mathbb{R}^{d_{l-1}}, \quad l \in [\kappa]$$

where $[n]$ denoting the set $\{1, \dots, n\}$. At the l -th layer, m_l and q_l denote the dimension of the signal, and the number of filter channel, respectively. The length of filter is assumed to be r .

We now define the l -th layer input signal for the encoder layer from q_{l-1} number of input channels

$$\mathbf{z}^{l-1} := \begin{bmatrix} \mathbf{z}_1^{l-1\top} & \dots & \mathbf{z}_{q_{l-1}}^{l-1\top} \end{bmatrix}^\top \in \mathbb{R}^{d_{l-1}},$$

where \top denotes the transpose, and $\mathbf{z}_j^{l-1} \in \mathbb{R}^{m_{l-1}}$ refers to the j -th channel input with the dimension m_{l-1} . The l -th layer output signal \mathbf{z}^l is similarly defined. Then, we have the following representation of the convolution and pooling operation at the l -th encoder layer [36]:

$$\mathbf{z}^l = \sigma(\mathbf{E}^{l\top} \mathbf{z}^{l-1}) \quad (\text{A.1})$$

where $\sigma(\cdot)$ is defined as an element-by-element ReLU operation $\sigma(x) = \max\{x, 0\}$, and

$$\mathbf{E}^l = \begin{bmatrix} \mathbf{\Phi}^l \circledast \psi_{1,1}^l & \dots & \mathbf{\Phi}^l \circledast \psi_{q_l,1}^l \\ \vdots & \ddots & \vdots \\ \mathbf{\Phi}^l \circledast \psi_{1,q_{l-1}}^l & \dots & \mathbf{\Phi}^l \circledast \psi_{q_l,q_{l-1}}^l \end{bmatrix} \quad (\text{A.2})$$

where $\mathbf{\Phi}^l$ denotes the $m_l \times m_l$ matrix that represents the pooling operation at the l -th layer, and $\psi_{i,j}^l \in \mathbb{R}^C$ represents the l -th layer encoder filter to generate the i -th channel output from the contribution of the j -th channel input, and \circledast represents a multi-channel convolution [36].

Similarly, the l -th decoder layer can be represented by [36]:

$$\tilde{\mathbf{z}}^{l-1} = \sigma(\mathbf{D}^l \tilde{\mathbf{z}}^l) \quad (\text{A.3})$$

where

$$\mathbf{D}^l = \begin{bmatrix} \tilde{\mathbf{\Phi}}^l \circledast \tilde{\psi}_{1,1}^l & \dots & \tilde{\mathbf{\Phi}}^l \circledast \tilde{\psi}_{1,q_l}^l \\ \vdots & \ddots & \vdots \\ \tilde{\mathbf{\Phi}}^l \circledast \tilde{\psi}_{q_{l-1},1}^l & \dots & \tilde{\mathbf{\Phi}}^l \circledast \tilde{\psi}_{q_{l-1},q_l}^l \end{bmatrix} \quad (\text{A.4})$$

where $\tilde{\mathbf{\Phi}}^l$ denotes the $m_l \times m_l$ matrix that represents the unpooling operation at the l -th layer, and $\tilde{\psi}_{i,j}^l \in \mathbb{R}^r$ represents

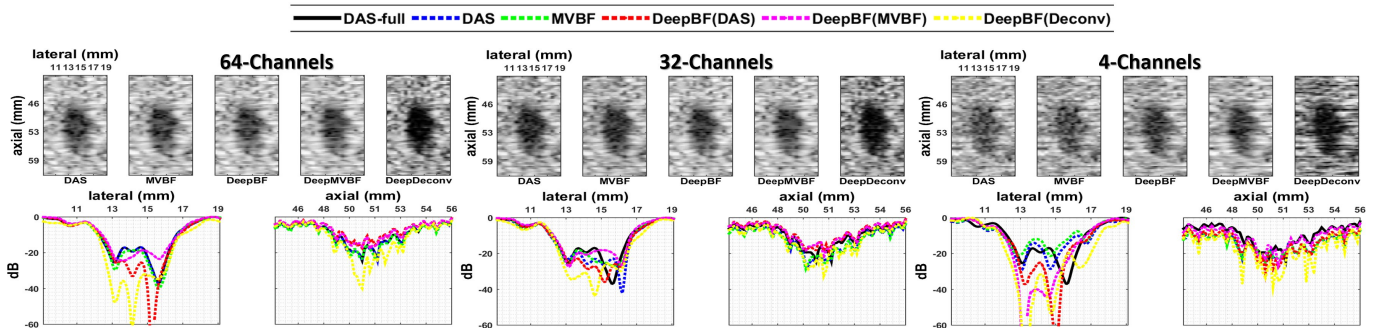


Fig. 12. Lateral and axial profiles across the depth through the center of the phantom 6 mm diameter anechoic cyst at 48 mm depth using DAS and various form of DeepBFs using random sampling patterns. Images are shown with a 60 dB dynamic range.

TABLE III
PERFORMANCE STATISTICS ON *in vivo* DATA FOR UNIFORM SAMPLING PATTERN

sub-sampling factor	CR (dB)			CNR			GCNR			PSNR (dB)			SSIM		
	DAS	MVBF	DeepBF	DAS	MVBF	DeepBF	DAS	MVBF	DeepBF	DAS	MVBF	DeepBF	DAS	MVBF	DeepBF
1	12.37	12.39	13.25	1.38	1.38	1.45	0.64	0.64	0.66	∞	∞	∞	1	1	1
2	10.69	10.74	12.50	1.21	1.20	1.37	0.60	0.59	0.64	22.69	22.74	24.91	0.85	0.85	0.90
2.7	10.24	10.34	11.97	1.15	1.16	1.31	0.58	0.58	0.63	21.36	21.44	23.18	0.80	0.81	0.86
4	9.67	9.80	11.00	1.10	1.10	1.22	0.56	0.56	0.60	20.08	20.19	21.38	0.75	0.76	0.80
8	9.25	9.40	9.97	1.04	1.05	1.11	0.54	0.54	0.56	18.63	18.75	19.10	0.68	0.69	0.70
16	9.08	9.25	9.58	1.02	1.03	1.08	0.53	0.53	0.55	17.84	17.95	17.83	0.63	0.63	0.64

TABLE IV
COMPARISON OF DIFFERENT DESIGN STRATEGIES WITH THE PROPOSED DEEPBF ON PHANTOM DATASET USING RANDOM SUB-SAMPLING PATTERN

Training/Design methods	CNR				GCNR				PSNR (dB)				SSIM			
	1 \times	2 \times	4 \times	8 \times	1 \times	2 \times	4 \times	8 \times	1 \times	2 \times	4 \times	8 \times	1 \times	2 \times	4 \times	8 \times
<i>RF-sum only</i>	2.256	2.320	2.302	2.171	0.842	0.863	0.873	0.857	∞	25.37	21.12	18.62	1	0.924	0.832	0.737
<i>fixed rate training</i>	2.325	2.505	2.341	2.121	0.850	0.890	0.883	0.853	∞	22.30	21.30	19.88	1	0.880	0.840	0.777
<i>single-depth design</i>	2.752	2.659	2.505	2.253	0.913	0.907	0.895	0.873	∞	27.92	23.57	19.27	1	0.930	0.852	0.739
<i>DeepBF(DAS)</i>	2.655	2.650	2.527	2.248	0.897	0.900	0.898	0.874	∞	28.24	24.55	21.27	1	0.946	0.878	0.783
<i>DeepBF(MVBF)</i>	2.701	2.666	2.523	2.306	0.905	0.904	0.897	0.876	∞	29.20	25.17	22.45	1	0.952	0.890	0.812

the l -th layer decoder filter to generate the i -th channel output from the contribution of the j -th channel input.

Next, consider the skipped branch signal χ^l by concatenating the output for each skipped branch as shown in Fig. 2. Then, the l -th encoder layer with the skipped connection can be represented by [36]:

$$\begin{bmatrix} z^l \\ \chi^l \end{bmatrix} = \begin{bmatrix} \sigma(E^{lT} z^{l-1}) \\ z^{l-1} \end{bmatrix} \quad (\text{A.5})$$

$$z^{l-1} = \sigma(D^l z^l + D^l \chi^l). \quad (\text{A.6})$$

With these definition, by following the derivation in [36], it is straightforward to show that the neural network output v is given by

$$v = \tilde{B}(z)B(z)z = \sum_i \langle b_i(z), z \rangle \tilde{b}_i(z) \quad (\text{A.7})$$

where Θ refers to all the convolution filter parameters, and $b_i(z)$ and $\tilde{b}_i(z)$ denote the i -th column of the matrices (A.8) and (A.9), respectively, which are defined as

$$B(z) = \begin{bmatrix} E^1 \Lambda^1(z) E^2 \dots \Lambda^{\kappa-1}(z) E^\kappa, \dots \\ \dots, E^1 \Lambda^1(z) \dots E^6, E^1 \Lambda^1(z) \dots E^3 \end{bmatrix} \quad (\text{A.8})$$

$$\tilde{B}(z) = \begin{bmatrix} D^1 \tilde{\Lambda}^1(z) D^2 \dots \tilde{\Lambda}^{\kappa-1}(z) D^\kappa, \dots \\ \dots, D^1 \tilde{\Lambda}^1(z) \dots D^6, D^1 \tilde{\Lambda}^1(z) \dots D^3 \end{bmatrix} \quad (\text{A.9})$$

where $\Lambda^l(z)$ and $\tilde{\Lambda}^l(z)$ denote the diagonal matrix with 0 and 1 values that are determined by the ReLU output in the previous convolution steps. Note that there are skipped connections at every third convolution operations in Fig. 2, so that the last blocks in (A.8) and (A.9) are indexed accordingly.

REFERENCES

- [1] F. Viola and W. F. Walker, "Adaptive signal processing in medical ultrasound beamforming," in *IEEE Ultrasonics Symposium, 2005.*, vol. 4, Sep. 2005, pp. 1980–1983.
- [2] J. Capon, "High-resolution frequency-wavenumber spectrum analysis," *Proceedings of the IEEE*, vol. 57, no. 8, pp. 1408–1418, Aug 1969.
- [3] F. Vignon and M. R. Burcher, "Capon beamforming in medical ultrasound imaging with focused beams," *IEEE Transactions on Ultrasonics, Ferroelectrics, and Frequency Control*, vol. 55, no. 3, pp. 619–628, March 2008.
- [4] K. Kim, S. Park, J. Kim, S. Park, and M. Bae, "A fast minimum variance beamforming method using principal component analysis," *IEEE Transactions on Ultrasonics, Ferroelectrics, and Frequency Control*, vol. 61, no. 6, pp. 930–945, June 2014.
- [5] W. Chen, Y. Zhao, and J. Gao, "Improved capon beamforming algorithm by using covariance matrix calculation," in *IET International Radar Conference 2013*, April 2013, pp. 1–6.
- [6] C. C. Nilsen and I. Hafizovic, "Beamspace adaptive beamforming for ultrasound imaging," *IEEE Transactions on Ultrasonics, Ferroelectrics, and Frequency Control*, vol. 56, no. 10, pp. 2187–2197, October 2009.
- [7] A. M. Deylami and B. M. Asl, "A fast and robust beamspace adaptive beamformer for medical ultrasound imaging," *IEEE Transactions on Ultrasonics, Ferroelectrics, and Frequency Control*, vol. 64, no. 6, pp. 947–958, June 2017.

- [8] A. C. Jensen and A. Austeng, "An approach to multibeam covariance matrices for adaptive beamforming in ultrasonography," *IEEE Transactions on Ultrasonics, Ferroelectrics, and Frequency Control*, vol. 59, no. 6, pp. 1139–1148, June 2012.
- [9] —, "The iterative adaptive approach in medical ultrasound imaging," *IEEE Transactions on Ultrasonics, Ferroelectrics, and Frequency Control*, vol. 61, no. 10, pp. 1688–1697, Oct 2014.
- [10] K. H. Jin, Y. S. Han, and J. C. Ye, "Compressive dynamic aperture b-mode ultrasound imaging using annihilating filter-based low-rank interpolation," in *2016 IEEE 13th International Symposium on Biomedical Imaging (ISBI)*. IEEE, 2016, pp. 1009–1012.
- [11] C. Schretter, S. Bundervoet, D. Blinder, A. Dooms, J. D'hooge, and P. Schelkens, "Ultrasound imaging from sparse rf samples using system point spread functions," *IEEE transactions on ultrasonics, ferroelectrics, and frequency control*, vol. 65, no. 3, pp. 316–326, 2017.
- [12] "Sub-nyquist sampling and fourier domain beamforming in volumetric ultrasound imaging," *IEEE Transactions on Ultrasonics, Ferroelectrics, and Frequency Control*, vol. 63, no. 5, pp. 703–716, May 2016.
- [13] N. Wagner, Y. C. Eldar, A. Feuer, G. Danin, and Z. Friedman, "Xampling in ultrasound imaging," in *Medical Imaging 2011: Ultrasonic Imaging, Tomography, and Therapy*, vol. 7968. International Society for Optics and Photonics, 2011, p. 796818.
- [14] E. Kang, J. Min, and J. C. Ye, "A deep convolutional neural network using directional wavelets for low-dose x-ray ct reconstruction," *Medical Physics*, vol. 44, no. 10, 2017.
- [15] E. Kang, W. Chang, J. Yoo, and J. C. Ye, "Deep convolutional framelet denoising for low-dose CT via wavelet residual network," *IEEE Transactions on Medical Imaging*, vol. 37, no. 6, pp. 1358–1369, 2018.
- [16] H. Chen, Y. Zhang, W. Zhang, P. Liao, K. Li, J. Zhou, and G. Wang, "Low-dose CT via convolutional neural network," *Biomedical Optics Express*, vol. 8, no. 2, pp. 679–694, 2017.
- [17] J. Adler and O. Öktem, "Learned primal-dual reconstruction," *IEEE Transactions on Medical Imaging (in press)*, 2018.
- [18] J. M. Wolterink, T. Leiner, M. A. Viergever, and I. Išgum, "Generative adversarial networks for noise reduction in low-dose CT," *IEEE Transactions on Medical Imaging*, vol. 36, no. 12, pp. 2536–2545, 2017.
- [19] K. H. Jin, M. T. McCann, E. Froustey, and M. Unser, "Deep convolutional neural network for inverse problems in imaging," *IEEE Transactions on Image Processing*, vol. 26, no. 9, pp. 4509–4522, 2017.
- [20] Y. Han and J. C. Ye, "Framing U-Net via deep convolutional framelets: Application to sparse-view CT," *IEEE Transactions on Medical Imaging*, vol. 37, no. 6, pp. 1418–1429, 2018.
- [21] S. Wang, Z. Su, L. Ying, X. Peng, S. Zhu, F. Liang, D. Feng, and D. Liang, "Accelerating magnetic resonance imaging via deep learning," in *Biomedical Imaging (ISBI), 2016 IEEE 13th International Symposium on*. IEEE, 2016, pp. 514–517.
- [22] K. Hammernik, T. Klatzer, E. Kobler, M. P. Recht, D. K. Sodickson, T. Pock, and F. Knoll, "Learning a variational network for reconstruction of accelerated MRI data," *Magnetic resonance in medicine*, vol. 79, no. 6, pp. 3055–3071, 2018.
- [23] J. Schlemper, J. Caballero, J. V. Hajnal, A. N. Price, and D. Rueckert, "A deep cascade of convolutional neural networks for dynamic MR image reconstruction," *IEEE Transactions on Medical Imaging*, vol. 37, no. 2, pp. 491–503, 2018.
- [24] B. Zhu, J. Z. Liu, S. F. Cauley, B. R. Rosen, and M. S. Rosen, "Image reconstruction by domain-transform manifold learning," *Nature*, vol. 555, no. 7697, p. 487, 2018.
- [25] D. Lee, J. Yoo, S. Tak, and J. Ye, "Deep residual learning for accelerated MRI using magnitude and phase networks," *IEEE Transactions on Biomedical Engineering*, 2018.
- [26] D. Allman, A. Reiter, and M. A. L. Bell, "A machine learning method to identify and remove reflection artifacts in photoacoustic channel data," in *2017 IEEE International Ultrasonics Symposium (IUS)*, Sept 2017, pp. 1–4.
- [27] A. C. Luchies and B. C. Byram, "Deep neural networks for ultrasound beamforming," *IEEE transactions on medical imaging*, vol. 37, no. 9, pp. 2010–2021, 2018.
- [28] M. Feigin, D. Freedman, and B. W. Anthony, "A deep learning framework for single sided sound speed inversion in medical ultrasound," *arXiv preprint arXiv:1810.00322*, 2018.
- [29] D. Perdios, A. Besson, M. Arditi, and J.-P. Thiran, "A deep learning approach to ultrasound image recovery," in *2017 IEEE International Ultrasonics Symposium (IUS)*. IEEE, 2017, pp. 1–4.
- [30] Z. Zhou, Y. Wang, J. Yu, Y. Guo, W. Guoand, and Y. Qi, "High spatial-temporal resolution reconstruction of plane-wave ultrasound images with a multichannel multiscale convolutional neural network," *IEEE transactions on ultrasonics, ferroelectrics, and frequency control*, 2018.
- [31] Y. H. Yoon, S. Khan, J. Huh, J. C. Ye *et al.*, "Efficient b-mode ultrasound image reconstruction from sub-sampled rf data using deep learning," *IEEE transactions on medical imaging*, 2018.
- [32] M. Gasse, F. Millioz, E. Roux, D. Garcia, H. Liebgott, and D. Friboulet, "High-quality plane wave compounding using convolutional neural networks," *IEEE transactions on ultrasonics, ferroelectrics, and frequency control*, vol. 64, no. 10, pp. 1637–1639, 2017.
- [33] O. Senouf, S. Vedula, G. Zurakhov, A. Bronstein, M. Zibulevsky, O. Michailovich, D. Adam, and D. Blondheim, "High frame-rate cardiac ultrasound imaging with deep learning," in *Medical Image Computing and Computer Assisted Intervention – MICCAI 2018*, A. F. Frangi, J. A. Schnabel, C. Davatzikos, C. Alberola-López, and G. Fichtinger, Eds. Cham: Springer International Publishing, 2018, pp. 126–134.
- [34] S. Vedula, O. Senouf, G. Zurakhov, A. Bronstein, M. Zibulevsky, O. Michailovich, D. Adam, and D. Gaitini, "High quality ultrasonic multi-line transmission through deep learning," in *Machine Learning for Medical Image Reconstruction*, F. Knoll, A. Maier, and D. Rueckert, Eds. Cham: Springer International Publishing, 2018, pp. 147–155.
- [35] J. C. Ye, Y. Han, and E. Cha, "Deep convolutional framelets: A general deep learning framework for inverse problems," *SIAM Journal on Imaging Sciences*, vol. 11, no. 2, pp. 991–1048, 2018.
- [36] J. C. Ye and W. K. Sung, "Understanding geometry of encoder-decoder CNNs," in *Proceedings of the 36th International Conference on Machine Learning*, ser. Proceedings of Machine Learning Research, K. Chaudhuri and R. Salakhutdinov, Eds., vol. 97. Long Beach, California, USA: PMLR, 09–15 Jun 2019, pp. 7064–7073.
- [37] S. Khan, J. Huh, and J. C. Ye, "Universal deep beamformer for variable rate ultrasound imaging," *arXiv preprint arXiv:1901.01706*, 2019.
- [38] B. Luijten, R. Cohen, F. J. de Bruijn, H. A. W. Schmeitz, M. Mischi, Y. C. Eldar, and R. J. G. van Sloun, "Deep learning for fast adaptive beamforming," in *ICASSP 2019 - 2019 IEEE International Conference on Acoustics, Speech and Signal Processing (ICASSP)*, May 2019, pp. 1333–1337.
- [39] D. H. Brandwood, "A complex gradient operator and its application in adaptive array theory," *IEE Proceedings F - Communications, Radar and Signal Processing*, vol. 130, no. 1, pp. 11–16, February 1983.
- [40] Z. Chen, A. Basarab, and D. Kouamé, "Compressive deconvolution in medical ultrasound imaging," *IEEE transactions on medical imaging*, vol. 35, no. 3, pp. 728–737, 2015.
- [41] J. A. Jensen, "Deconvolution of ultrasound images," *Ultrasonic imaging*, vol. 14, no. 1, pp. 1–15, 1992.
- [42] M. O'Donnell, E. Jaynes, and J. Miller, "Kramers–Kronig relationship between ultrasonic attenuation and phase velocity," *The Journal of the Acoustical Society of America*, vol. 69, no. 3, pp. 696–701, 1981.
- [43] J. Duan, H. Zhong, B. Jing, S. Zhang, and M. Wan, "Increasing axial resolution of ultrasonic imaging with a joint sparse representation model," *IEEE Transactions on Ultrasonics, Ferroelectrics, and Frequency Control*, vol. 63, no. 12, pp. 2045–2056, Dec 2016.
- [44] A. Vedaldi and K. Lenc, "Matconvnet: Convolutional neural networks for Matlab," in *Proceedings of the 23rd ACM international conference on Multimedia*. ACM, 2015, pp. 689–692.
- [45] X. Glorot and Y. Bengio, "Understanding the difficulty of training deep feedforward neural networks," in *Proceedings of the Thirteenth International Conference on Artificial Intelligence and Statistics*, 2010, pp. 249–256.
- [46] J. F. Synnevag, A. Austeng, and S. Holm, "Adaptive beamforming applied to medical ultrasound imaging," *IEEE Transactions on Ultrasonics, Ferroelectrics, and Frequency Control*, vol. 54, no. 8, pp. 1606–1613, August 2007.
- [47] R. M. Rangayyan, *Biomedical Image Analysis*, ser. Biomedical Engineering, M. R. Neuman, Ed. Boca Raton, Florida: CRC Press, 2005.
- [48] A. Rodriguez-Molares, O. M. H. Rindal, J. D'hooge, S.-E. Måsøy, A. Austeng, and H. Torp, "The generalized contrast-to-noise ratio," 2018.
- [49] Z. Wang, A. C. Bovik, H. R. Sheikh, and E. P. Simoncelli, "Image quality assessment: from error visibility to structural similarity," *IEEE Transactions on Image Processing*, vol. 13, no. 4, pp. 600–612, April 2004.